

**Published in Volume 16, Number 17, 20 November 1995.**

## **C-band Backscatter Measurements of Winter Sea Ice in the Weddell Sea, Antarctica**

**Mark R. Drinkwater<sup>†</sup>**

Jet Propulsion Laboratory  
California Institute of Technology  
4800 Oak Grove Drive  
CA 91109, USA

**Reza Hosseinmostafa and Prasad Gogineni**

Radar Systems and Remote Sensing Laboratory  
University of Kansas Center for Research Inc.  
2291 Irving Hill Road  
Lawrence, KA 66045, USA

<sup>†</sup> Present Address as Visiting Scientist: Alfred Wegener Institut für Polar- und Meeresforschung, Am Handelshafen 12, D-27570 Bremerhaven, Germany.

# C-band Backscatter Measurements of Winter Sea Ice in the Weddell Sea, Antarctica

Mark R. Drinkwater  
Jet Propulsion Laboratory,  
California Institute of Technology  
4800 Oak Grove Drive  
CA 91109, USA

Reza Hosseinmostafa and Prasad Gogineni  
Radar Systems and Remote Sensing Laboratory  
University of Kansas Center for Research Inc.,  
2291 Irving Hill Road  
Lawrence, KA 66045, USA

**Abstract.** During the 1992 Winter Weddell Gyre Study, a C-band scatterometer was used from the German ice-breaker *R/V Polarstern* to obtain detailed shipborne measurement scans of Antarctic sea ice. The frequency-modulated continuous-wave (FM-CW) radar operated at 4.3 GHz and acquired like- (VV) and cross-polarization (HV) data at a variety of incidence angles ( $10\text{--}75^\circ$ ). Calibrated backscatter data were recorded for several ice types as the icebreaker crossed the Weddell Sea and detailed measurements were made of corresponding snow and sea ice characteristics at each measurement site, together with meteorological information, radiation budget and oceanographic data. The primary scattering contributions under cold winter conditions arise from the air/snow and snow/ice interfaces. Observations indicate some similarities with Arctic sea ice scattering signatures although the main difference is generally lower mean backscattering coefficients in the Weddell Sea. This is due to the younger mean ice age and thickness, and correspondingly higher mean salinities. In particular, smooth white ice found in 1992 in divergent areas within the Weddell Gyre ice pack was generally extremely smooth and undeformed. Comparisons of field scatterometer data with calibrated  $20\text{--}26^\circ$  incidence ERS-1 radar image data show close correspondence, and indicate that rough Antarctic first-year and older second-year ice forms do not produce as distinctively different scattering signatures as observed in the Arctic. Thick deformed first-year and second-year ice on the other hand are clearly discriminated from younger undeformed ice, thereby allowing successful separation of thick and thin ice. Time-series data also indicate that C-band is sensitive to changes in snow and ice conditions resulting from atmospheric and oceanographic forcing and the local heat flux environment. Variations of several dB in  $45^\circ$  incidence backscatter occur in response to a combination of thermally-regulated parameters including sea-ice brine volume, snow and ice complex dielectric properties, and snow physical properties.

**Key Words:** C-band Scatterometer, Antarctic Sea Ice, Microwave Scattering, Surface Fluxes

## **1. Introduction**

Annual growth of Southern Ocean sea ice over an area of about 20 million km<sup>2</sup> requires that spaceborne microwave remote sensing be employed as the only practical method to monitor the extent and characteristics of this winter Antarctic sea ice cover. Formation of an extensive ice cover around Antarctica is intimately linked to water mass modification and blending processes by salinating the upper ocean and creating buoyancy gradients. Resulting vertical thermohaline fluxes and large-scale circulation within the zone between the Antarctic polar front and the continental margin together influence the overall hydrographic characteristics of the Southern Ocean (Gordon and Huber 1990). Observations and theory confirm that the marginal stability of the winter mixed layer in regions such as the Eastern Weddell Sea can be upset by a modest increase in the salt flux from enhanced sea-ice formation in leads and polynyas. Such sea ice features represent holes in the insulating sea ice blanket and can modulate the horizontal and vertical thermohaline and freshwater fluxes of this region. Significant convective events such as that revealed by the Weddell Polynya (Carsey 1980, Gordon 1991) released large amounts of heat and moisture into the atmosphere and provided sufficient enhancement of cooling and ventilation for the production of Antarctic Bottom Water. Knowing the regional distribution of open water and thus new ice formation in the ice pack is a critical scientific requirement with respect to accurate calculations of horizontal and vertical thermohaline fluxes in the Southern Ocean.

Satellite-borne microwave radars will yield uninterrupted sea-ice coverage over both polar regions for the next decade and beyond (Carsey *et al.* 1992). Currently, the 5.3 GHz (C-band) ERS-1 synthetic aperture radar (SAR) is the only instrument capable of acquiring high-resolution (20m) image data of Antarctic sea-ice on an all-weather (day or night), frequent repeat basis. However, this dataset is limited to areas covered by existing receiving stations. As an alternative, the ERS-1 scatterometer data enables generation of an intermediate resolution image product (12 km) covering the entire Southern Ocean (Drinkwater *et al.* 1993a). In this paper we compare field-measured backscattering signatures acquired in regions of different ice characteristics with coincident images from the ERS-1 SAR. The ultimate scientific goal is to use the tools which microwave remote sensing offers to evaluate the relationship between the changing basin-wide distribution of sea ice and surface fluxes of heat, salt, freshwater and momentum.

## **2. The Winter Weddell Gyre Study**

The Winter Weddell Gyre Study (WWGS '92) was the second austral winter experiment in a series of ongoing investigations of the Weddell Gyre. It was conducted by German, U.S., English and Canadian investigators on-board the German ice-breaking research vessel *R/V Polarstern*. One unique element of this cruise was that it was conducted with simultaneous

observations by the ERS-1 satellite SAR and Scatterometer. This was the first ever active microwave image data to be recorded of winter sea ice in Antarctica by a satellite-borne radar.

## 2.1 Satellite Image Data

The ERS-1 spacecraft routinely collected data over the WWGS '92 study region shown in Figure 1. The active microwave instrument (AMI) acquired data in its SAR and Wind Scatterometer modes. The former is a high-bit-rate data stream requiring direct downlink to and recording at the nearest ground receiving station. SAR data acquisition throughout the experiment (between June and August) was facilitated by the German Antarctic Receiving Station (GARS) at the *General Bernardo O'Higgins* Base, which is located at the northern end of the Antarctic peninsula. During satellite data acquisition a program of shipborne active and passive microwave observations, coupled with *in-situ* measurements, allowed investigation of the microwave backscatter signatures of various types of Antarctic sea ice.

## 2.2 Field Scatterometer and Sea-Ice Surface Measurements

A University of Kansas C-band field-scatterometer instrument (Figure 2) was operated during WWGS '92 from the port rail of *R/V Polarstern* to measure microwave backscattering characteristics of Antarctic sea ice. When the ship was stationary in sea ice, the radar was scanned to obtain independent samples of sea-ice backscatter coefficient ( $\sigma^0$ ) as a function of incidence angle ( $\theta$ ) and polarization. Detailed measurements were made within the radar footprint each time a radar scan was completed so as not to disturb the surface. Measurements were made of the physical, chemical and dielectric properties of the snow and sea ice, and of the surface heat fluxes. Field sampling at stopping points along the ship track provided validation data for simultaneous satellite ERS-1 C-band SAR observations (at  $20^\circ \leq \theta \leq 26^\circ$ ) and enabled collection of a catalogue of 'snap-shot' microwave signatures at known locations (Drinkwater and Haas 1994).

Short 3-4 hour ice stations at the sites shown in Figure 1 enabled radar and snow and ice measurements of a number of ice types characteristic of the winter Weddell Sea ice cover (Drinkwater *et al.* 1993b). A 3-day long ice station from 21-24 July, 1992, also enabled time-series  $\sigma^0$  measurements. In addition to periodic scans over the complete range of incidence angles, the radar was operated at frequent intervals (every 4 hours) at  $\theta = 45^\circ$ . At this angle  $\sigma^0$  is sensitive to the surface reflectivity and roughness, and also to volume scattering within the snow and ice surface. These data quantify changes in  $\sigma^0$  as the physical properties of the snow and ice changed in response to variations in the heat flux and vapour flux regime. Examples of data from these stations are shown in the following sections.

## 3. **The Radar Scatterometer**

The University of Kansas scatterometer is a low power, triple-antenna, FM-CW (frequency-modulated, continuous-wave) radar altimeter modified to perform ship-mounted backscatter measurements (see Table 1). It operates at a C-band center frequency of 4.3 GHz (i.e.  $\lambda = 6.98$  cm) and was configured for like- (VV) and cross-polarized (HV) measurements. The antenna cluster consisted of a parabolic dish transmitting antenna fixed at vertical linear polarization, a horn antenna for receiving linear like-polarized signals, and a stripline antenna for receiving cross-polarized signals. This cluster was mounted orthogonal to the ship's rail facing to port (see Figure 2) and was fixed in azimuth but hinged and steerable in the elevation plane by an actuator. A pendulum, fixed in an orientation boresighted with the antennas, provided a simple digital readout calibrated to incidence angle, enabling measurements at precise incidence angles ( $10^\circ \cdot \theta \cdot 75^\circ$ ) from a workstation inside the ship. The height above the sea ice surface varied as a function of the ship's draft on a day to day basis, with a mean height  $H = 16.7$  m.

The scatterometer system is divided physically into two parts: a transmitter/receiver section, and a data acquisition section. The former was located in a weatherproof box directly behind the antenna plate (Figure 2) to minimize the power loss through cables linking the antenna feeds and the transmitter/receiver unit. The received signals are carried along cables to the data acquisition system located in an indoor work area. A block diagram of the system is shown in Figure 3.

### 3.1 Transmitter and Receiver Subsystem

Output from the transmitter is frequency-modulated using a triangular wave function. This signal is subdivided into two parts: the first part is fed into the local oscillator port of the mixer, and the second is mixed with a fixed delay-line and coupled into calibration loops. The calibration loop, consisting of calibration IF input from the mixer, IF gain stages, and the modulator, controls the modulation rate to maintain constant calibration IF frequency. The remaining portion of the transmitted signal propagates from the transmitting antenna through space to the target where some of its energy is scattered back in the direction of the radar. This backscattered signal is collected by the receiving antenna and down-converted, filtered, amplified and fed into the data acquisition section of the radar system.

### 3.2 Data Acquisition Subsystem

The radar was controlled by a Texas Instruments personal computer (PC) equipped with a special Digital Signal Processing (DSP) board and the data were stored digitally on hard disk by the PC and independently by a Hewlett Packard Signal Analyser (HP35680A). The signal analyser provided the magnitude and phase of the signal recorded by the PC together with independent data storage. Recorded data were processed and viewed in real-time using the DSP board and the bandwidth could be selected to optimise the range resolution. The recorded signal was band-pass filtered to separate the target from the background clutter and converted to

independent samples of received power. Direct measurements of the transmitted and received power spectra were recorded on the PC and Signal Analyser for subsequent use in post-processing and calibration of the data.

### 3.3 Backscatter Measurements

Recorded values of received power  $P_r$  are converted into normalised backscatter coefficient,  $\sigma^\circ$  (i.e. cross-section per unit area) during post-processing, utilising corresponding records of the transmitter power  $P_t$ , and the range  $R$  to the target area at an incidence angle  $\theta$ . For each measurement, a number of corrections are first made to account for the scatterometer beam characteristics and physical configuration of the system, and to calibrate the measurements.

#### *Beam Pattern Corrections*

Measurements are corrected for the shape of the beam of the transmitting and receiving antennas and for their impact upon the illuminated area. The radar equation for an extensive target is generalised assuming that  $\sigma^\circ$  is independent of the azimuth angle  $\phi$  and that  $P_r$  comes from the target area illuminated within the antenna half-power beamwidths  $\beta_a$  and  $\beta_e$  (after Gogineni *et al.* 1990)

$$P_r = \frac{P_t G_{t \max} G_{r \max} \lambda^2}{(4\pi)^3} \int_{-\beta_a/2}^{\beta_a/2} \int_{-\beta_e/2}^{\beta_e/2} \frac{g_t g_r \sigma^\circ(\theta, \phi)}{R^4} dA \quad (1)$$

where subscripts  $a$  and  $e$  refer to the azimuth (H-plane) and elevation (E-plane) of the antennas (details given in Table 1),  $G_{t \max}$  and  $G_{r \max}$  are the maximum gains, and  $g_t$  and  $g_r$  the relative gain functions of the transmit and receiving antennas, respectively. A narrow-beam assumption is then made by considering the variables constant over the illuminated area  $A_t$ , then

$$P_r = \frac{P_t G_{t \max} G_{r \max} \lambda^2 \sigma^\circ A_t}{(4\pi)^3 R^4} \quad (2)$$

To derive the backscatter, (2) is substituted for  $P_r$  in (1) to give

$$\sigma_t^\circ = \frac{R_0^4 \int_{-\beta_a/2}^{\beta_a/2} \int_{-\beta_e/2}^{\beta_e/2} \frac{g_t g_r \sigma_m^\circ}{R^4} dA}{A_t} \quad (3)$$

where  $\sigma_m^\circ$  is the measured scattering coefficient and  $\sigma_t^\circ$  is the true scattering coefficient. The gain functions for the mainlobe antenna patterns of the paraboloid and horn antennas approximate to circular Gaussian functions of the form

$$g(\theta) = e^{\left\{-k\left(\frac{\theta}{\beta}\right)^2\right\}} \quad (4)$$

where  $\theta$  is the incidence angle ( $^\circ$ ) and  $\beta$  is the effective half-power beamwidth of the antenna. The constant  $k$  which describes the circular Gaussian antenna patterns (whose characteristics are given in Table 1) is 2.75, and the form of the beam patterns is shown in Figure 4. The radar beam projected onto the surface illuminates an area  $A_I$  in (3) which changes with  $\theta$  and as a function of range and ship rail height (Figure 4). The spherical Gaussian beam pattern is elongated in the range direction to form an extended ellipse whose dimensions depend on  $\beta$  and  $\theta$ . For a circular beam projected onto the surface, the area is

$$A_I = \frac{\pi H^2 \beta^2}{4 \cos^3(\theta_i)}. \quad (5)$$

#### *Beam Overlap Correction*

The V-pol antennas used for transmit and receive are not perfectly aligned and have non-identical beam patterns. Furthermore, they are separated by a small distance (0.5 m) in the horizontal plane (H-plane). At close range and incidence angles near nadir the beam spot overlap is at its minimum, due to the reduced range and the smaller spot size. The fact that the beam patterns do not overlap perfectly requires a correction to the area  $A_I$  in the radar equation: the greater the range the larger the beam overlap and the smaller the correction factor. For parallel Gaussian beams this correction factor  $C_h$  is (Moore 1985)

$$C_h = \exp\left\{\frac{-s_h^2 k^2}{\beta_h^2 R^2 (1 + m_h^2)}\right\} \quad (6)$$

where  $s_h$  is the horizontal separation of the antennas,  $k$  is a constant,  $m_h$  is the ratio of the transmit and receive antenna beam widths and the subscript  $h$  refers to the horizontal plane. Each of the antennas point at identical incidence angles and there is no effective separation in the elevation plane: thus no correction factor is needed for the vertical plane. Figure 4 shows that as incidence angle and range increase, the illuminated area from the narrower paraboloid beam becomes increasingly closer to the centre of the collecting horn antenna and the resulting correction factor  $C_h$  varies as a function of incidence angle. For a height above the surface of 17m, and values of  $m_h = 0.35$ ,  $\beta_h = 0.139$  rad,  $s_h = 0.5$  m, and  $k = 2.75$ , from (6),  $C_h$  increases from -1.15 dB at  $20^\circ$  to a value of -0.23 dB at  $65^\circ$ .

### 3.4 Data Calibration

During the experiment the radar was to an extent internally self-calibrating. The system contained a loop controlling the period of the calibrator local oscillator source, such that the

calibration IF frequency is maintained at 2.5 kHz. The period and center frequency of the internal calibration signal was monitored and recorded using the HP Signal Analyser throughout the experiment in order to document the consistency of the scatterometer measurements.

### *Internal Calibration*

Internal calibration during post-processing uses the 'feed-through' signal to correct for variations in transmitted power. This signal is coupled through the antennas because of finite isolation between transmit and receive antennas. We range-gated the measured signal to isolate the feed-through signal by passing it through a low-pass filter with a cut-off frequency of 1 kHz. We then computed the average power within the filter passband. The daily average of the gated power was within  $\pm 1.5$  dB of the mean value from June 25 - July 28, 1992 (Julian Days 177 - 210), indicating that the radar is relatively stable (see Figure 5a).

In general, returned power from a distributed target varies as  $1/R^2$ , where  $R$  is the range to the target. Thus, as the range doubles, the returned power from a distributed target falls-off at 6 dB/octave. However, in the radar system the IF signal passes through a single pole high-pass filter with a 6 dB/octave slope to eliminate  $R^2$  dependence of the received power. The cut-off frequency of the high-pass filter is at 80 kHz. We removed the effect of the IF gain by passing the signal through a low-pass filter with the cut-off frequency of 80 kHz. Figure 5b compares the measured backscattering coefficient from sea ice as a function of incidence angle with and without use of the low-pass filter. The resulting correction increases the scattering coefficient by up to 4 dB at high incidence angles while reducing it by a smaller amount at low angles.

### *External Calibration and Signal to Noise*

Periodic external calibrations were performed by measuring the received power from a standard 12" Luneberg Lens placed on the surface at varying range. This target was used at several sites throughout the experiment to test the system signal-to-noise ratio (snr) over various ice types and to enable conversion of power data into scattering coefficients. The theoretical maximum scattering cross-section of the lens (for  $\lambda = 6.98$  cm) is  $\sim 11$  dBm<sup>2</sup>, but performance degradation over its lifetime resulted in a measured reference cross section of 7 dBm<sup>2</sup> (made before the experiment). In addition, the lens is used to obtain an snr estimate from the system. The ratio of backscatter cross section from a spot of area  $A$ , to the lens cross-section  $\sigma_{lens}$ , from the radar equation is

$$\frac{P_{in}}{P_{lens}} = \frac{\sigma^o A}{\sigma_{lens}}. \quad (7)$$

If  $\sigma_{lens}$  is 7 dBm<sup>2</sup>, the peak power in the spectrum from the lens measurement 10 dB, and the illuminated area 10 m<sup>2</sup> (at  $\theta = 45^\circ$ ), then the *snr* is calculated by rearranging terms in (7) and expressing power in dB



$$\sigma_{dB}^o = P_{in} - P_{lens} + \sigma_{lens} - 10 \log_{10}(A). \quad (8)$$

When the noise floor power  $P_{noise}$  is substituted for the input power  $P_{in}$  then we get a noise equivalent backscatter cross-section of  $\sigma_{noise}^o \bullet -43$  dB. For a target of known cross-section such as the lens there is an error in calibration associated with the fact that the measured backscatter  $\sigma_{in}$  is a combination of the desired field of the calibration target  $\sigma_c$  and the surrounding background clutter  $\sigma_b$ . Thus the resulting maximum calibration error is

$$\frac{\sigma_{in} - \sigma_{lens}}{\sigma_{lens}} = \frac{\sigma_b}{\sigma_{lens}} \pm 2 \sqrt{\frac{\sigma_b}{\sigma_{lens}}}. \quad (9)$$

If the value of  $\sigma_b/\sigma_{lens}$  is -43 dB as estimated above from lens calibrations, then the resulting maximum possible calibration error is  $\pm -18.5$  dB, or equivalently about 1.5% error, and is considered negligible.

#### 4. WWGS '92 Scatterometer Measurements

The objective of this investigation was to obtain a detailed microwave backscatter signature dataset and to collect validation data for ERS-1 C-band SAR observations of Weddell Sea ice. At short ice stations combined radar and snow and ice measurements were made of a number of ice types characteristic of the Weddell Sea during the wintertime (Viehoff *et al.* 1993; Haas *et al.* 1992). These included undeformed, snow-covered grey (10 - 30 cm thick) and white (30 - 70 cm thick) first-year ice, and second-year and former fast ice floes (exceeding 200 cm thickness) each with extreme snow loading. Other deformed ice types included ridged and rafted white ice and hummocked second-year floes. The following discussion gives a broad description of typical mean signatures observed during the WWGS '92 transect from sample sites shown in Figure 1.

##### 4.1 First-year Ice Signatures

Previous winter C-band signature examples from the Weddell Sea are limited and observations from WWGS '92 shown in this paper highlight a number of differences, and indicate a greater range of signatures than previously documented by Hosseinmostafa *et al.* (1994). The following examples illustrate scatterometer data acquired at individual sites, and a number of mean signatures from ice with similar salinity, thickness, and roughness characteristics. Additional information on snow and ice characteristics are provided in Drinkwater and Haas (1994) for each site. Graphs showing data from individual sites (with a single measurement set) have points corresponding to the mean of several independent samples at each incidence angle. In cases where averages are constructed from measurements at several sites, symbols indicate the mean values together with error bars corresponding to  $\pm 1\sigma$ . In either case, a least-squares logarithmic

curve is fitted to the mean values to illustrate the trend in the radar backscatter signatures.

### *Young Ice*

*Polarstern* encountered the ice edge on 10 June, 1992. Extensive pancake ice was observed for the majority of this southbound leg of WWGS'92 as *Polarstern* traversed an extensive marginal ice zone several hundred kilometers wide. The first observations of pancake ice with the C-band scatterometer were made on 12 June. Figure 1 indicates these locations by crosses along the Greenwich ( $0^\circ$ ) meridian. Figure 6a shows two distinctly different pancake ice signatures from 13 and 14 June, for similar ice thicknesses of 10-15 cm. The main characteristic of each signature is the shallow fall-off of the radar backscatter with incidence angle: both signatures exhibit extremely high values of  $\sigma^\circ$  exceeding -20 dB at all angles less than  $50^\circ$  incidence. Backscatter signatures for the two days differ by 15 dB at high incidence angles and appear dependent upon the roughness of the upturned edges of the cakes, the degree of compactness of the ice pans, and the degree of wave washing of the individual ice pans. Pancake ice on 13 June was distinctly different exhibiting greater surface roughness and wave washing, and lower ice concentrations than observed further south on 14 June. Also, in the case of the more southerly location, pancakes had a shallow snowcover which reduces the surface reflection coefficient from values more typical of wave-washed bare pancakes. Drinkwater *et al.* (1993a) show ERS-1 C-band scatterometer images of the ice edge in this location during June, also observing that the backscatter at  $40^\circ$  often exceeds -10 dB. Furthermore, it is typical in these ERS-1 scatterometer images to observe a bright fringe of pancake ice around the outer ice edge of the marginal ice zone in this location due to the higher energy wave environment and the lower ice concentrations.

The consolidation of a young ice sheet into first nilas (< 1cm thick) and then grey and white ice was observed in the shore polynya systems along the coast of Antarctica (Figure 1) and along the transect across the Weddell Sea in divergent regions of the ice pack. The average of all white ice observations (of 30 - 70 cm thick ice) is shown in Figure 6b. This mean signature indicates a more rapid fall-off in  $\sigma^\circ$  than data shown by Hosseinmostafa *et al.* (In press) and is likely because this is thinner, smoother and younger than the smoothest first-year ice they observed later in the ice-growth season. Many of these white ice observations were made of extremely smooth ice with little rafting or ridging, and the values of  $\sigma^\circ$  of below -25 dB appear typical of the lowest values of backscatter observed by ERS-1 at  $20$ - $26^\circ$  incidence angle for smooth, young first-year ice in the Arctic (Kwok and Cunningham 1994). Also of note for this high salinity young ice are the low cross-polarized signatures of around -40 dB. This appears typical of relatively smooth, recently formed ice which has observed surface salinities of the order of 20 % or higher. The dominance of surface scattering from smooth, young ice also accounts for the relatively rapid decay of  $\sigma^\circ$  with incidence angle of 0.4 dB/deg in the  $20$  -  $70^\circ$  range.

### *Medium-thick first-year ice*

By far the most predominant type of ice observed throughout the cruise was ice between 50 cm and 75 cm thick. This ice was observed under rapid growth conditions during WWGS '92 in coastal polynya systems. During a period spent stationary in recently formed ice, this smooth, and fairly undeformed young ice was observed to ridge around the vessel during a storm. Measurements were made with the scatterometer both before and after the deformation 'event' and these signatures are compared in Figure 7. The 21 June curve shows a fit to the single data scan acquired before the storm and the scan on the following day (22 June) represents the ridged ice. Surface characteristics and the degree of ridging were inhomogeneous across the transect scanned by the radar, resulting in the variability in the signature values. For comparison, the mean signature of smooth first-year ice for the entire experiment is shown in Figure 8. The data in Figure 7 show a less rapid fall-off of 0.3 dB/deg, than the mean smooth ice in Figure 8 (0.65 dB/deg.), but values are typical of ERS-1 values on the order of between -10 and -20 dB. Cross-polarized values show little incidence angle dependence, varying between -35 and -38 dB. These 20 - 26° incidence range values correspond closely with the typical backscattering behaviour of undeformed Arctic first-year ice presented by Kwok and Cunningham (1994). But, the decay in backscatter shows a much steeper fall-off with incidence than for comparative ice forms in the Arctic. This mean signature, for ice with typically small characteristic surface roughness, is characteristic of ice formed in divergent ice regions away from the coastline and such ice is typical of the central Weddell Sea.

### *Rough and deformed first-year ice*

The mean signature of rough first-year ice is described by Figure 9a, and is associated with deformed medium-thick first-year ice where ridging or rafting is not particularly intense (with ridge sail heights generally lower than 1 m). However, this mean signature is biased because little heavily ridged ice was observed during the transect across the central Weddell Sea. Most rough ice forms was observed in the coastal deformation region in the Eastern Weddell Sea which provided little access to the ship, and consequently could not be observed with the scatterometer. Thus, the signature in Figure 9a is not representative of the roughest ice observed during WWGS'92 or indeed in the entire Weddell Sea in winter. This translates particularly into low values at the higher incidence angles. The rough ice signature shown in Figure 7 indicates the relative extreme observed in more intensely deformed areas of first-year ice, and when compared with Figure 9a indicates the bias to a low mean value at high incidence angles. Nonetheless, the mean backscatter in the ERS-1 incidence-angle range is between approximately -10 and -16 dB which agrees favourably with the Arctic ERS-1 observations of deformed first-year ice made by Kwok and Cunningham (1994).

## 4.2 Second-year Ice

Figure 9 compares the mean rough first-year ice signature (a) with the mean old ice or second-year ice signature (b). These two mean signatures are extremely similar in character and are almost identical in magnitude and gradient. This confirms results shown by Hosseinmostafa *et al.* (1994) who also state that discrimination of rough first-year and second-year ice is difficult on the basis of backscatter coefficient at a specific incidence angle. The only discriminating feature is that the backscatter at higher incidence angles tends to be slightly lower for mean rough first-year ice (Figure 9a). However, this difference would be negligible if examples of rougher first-year ice had been sampled. Notwithstanding this observation, all second-year floes observed during WWGS '92 had extremely deep, layered snow covers (1-2 m in depth), similar to cases previously observed by Wadhams *et al.* (1987). In all cases, this snow exhibited complex layered stratigraphies with evidence of previous summer melt and seasonal temperature cycling. Typical characteristics were clear depth hoar and ice layer strata, with ice lenses and vertical ice pipes observed in some places across the surface snowcover of these floes. Thus, in the absence of a low-salinity bubble-rich surface layer (as observed to be important for Arctic multiyear ice volume scattering) internal snow layer and snow volume scattering from old snow upon second-year ice appears to be responsible for elevated backscattering at high incidence angles. This is in direct contrast to the predominant snow/ice interface scattering occurring from rough first-year floes in Figure 9a.

## 5. **ERS-1 Calibrated Backscatter Results**

Calibrated SAR and Scatterometer-derived  $\sigma^0$  values from the ERS-1 Active Microwave Instrument show good correspondence with the results shown in the previous section. Figure 10 shows a summary of SAR image histogram statistics derived from three regions of contrasting winter ice conditions in the Weddell Sea from Drinkwater *et al.* (1994). The three images were acquired on 6, 12, and 17 July, 1992, in regions correspond to uniform areas of deformed coastal first-year ice in the Eastern Weddell Sea (i.e. rough first-year), undeformed white ice in the central Weddell Sea (i.e. smooth first-year), and mixed deformed and undeformed first-year and second-year ice (i.e. first-year/second-year) in the north-western Weddell Sea. Their center-point coordinates are 72°S 13°W, 67°S 26°W, and 64°S 42°W, for rough first-year, smooth first-year, and mixed ice respectively (see Figure 1). In Figure 10, peaks in each of the single component distributions closely reflect the 20 - 26° incidence angle field-scatterometer data values shown in the previous section. These data appear to show that the mixed deformed and undeformed histogram is a simple combination of the individual distributions of the components of first-year and second-year ice (or deformed first-year ice) in proportions determined by their relative concentration. Similarly, the histograms indicate that the scatterometer values plotted for smooth first-year ice in the previous section fill only the lower portion of the distribution function. Clearly, field scatterometer measurement of young first-year ice is restricted to small areas of

smooth ice, which may otherwise be too small to be measured by the 30m resolution SAR. Mixed SAR pixels result therefore in a smooth first-year ice signature mean of -13 dB, which is slightly higher than most field-measured scatterometer values measured in this incidence angle range.

ERS-1 SAR backscatter data indicate that discrimination of rough first-year and second-year ice is difficult due to similarities in their backscatter in the 20 - 26° range. The field scatterometer measurements shown in this paper support this conclusion. However, discrimination of thick versus thin ice is a more critical task from the perspective of estimating ice mass or freshwater flux in the Weddell Sea. Scatterometer signatures and to a lesser extent ERS-1 SAR histograms demonstrate that discrimination of the principal categories of thick deformed first-year (or second-year) and smooth undeformed first-year or white ice is a fairly simple task. Multiple incidence angle measurements made by a scatterometer are also more adept at separating ice types than the limited incidence angle range provided by ERS-1 SAR. ERS-1 scatterometer measurements may therefore be more valuable for monitoring the relative areal extents of thick and thin ice (Grenfell *et al.* 1992, Martin *et al.* 1992). In contrast, SAR enables more detailed high resolution estimates of the lead fraction or amount of undeformed versus deformed ice in a given region, or indeed tracking of this ice through the growth season (Drinkwater and Kottmeier 1994).

## **6. Time-Series Backscatter Data**

### **6.1 Drift Station Measurements**

A drifting station conducted between 21:00hrs on 21 July (day 203) and 16:00 on 24 July, 1992 (day 206), offered the possibility of making time-series observations with the field scatterometer, as described in Section 2.2. Large temperature changes recorded during stormy weather at this ice station enable an investigation of links between microwave signature characteristics and the meteorological conditions controlling the surface-energy balance. For determination of the energy budget, the University of Hannover continuously measured the radiation components, turbulent fluxes of sensible and latent heat, and the conductive heat flux through the sea ice and snow cover (see Lemke, 1994; pages 40-49) for a total of over 60 hours of data (courtesy of W. Frieden of Hannover University, Germany). Measurements of the incoming short- and long-wave radiation were made with a CM-11 Kipp and Zoenen pyranometer and Epply pyrgeometer, respectively. Outgoing long-wave radiation was measured with a KT-4 radiation-thermometer and reflected short-wave with a downward-looking pyranometer, so that the albedo can be directly calculated. Turbulent fluxes were characterised using measurements from a Metek sonic anemometer thermometer mounted on the ship's boom. A series of 10-minute averages are computed from the original 10 Hz sampled data stream, which yield direct estimates of the

kinematic wind stress and the components of the wind, and a measure of the turbulent flux of sensible heat.

## 6.2 Initial Snow and Ice Conditions

The location selected for the long ice station was in extensive smooth, 105 cm thick, undeformed, snow-covered first-year sea ice formed in a large lead (at 62°20.5'S 43°41.1'W). Although the upper 13 cm of the ice comprised porous frazil ice, over 60% of sampled ice core lengths comprised congelation ice, indicating past growth under quiescent conditions (Drinkwater and Haas 1994). The ice surface had previously undergone melting, as evidenced by a reversed salinity gradient in the upper strata and an accompanying smooth layer of meteoric snow-ice of ~1cm thickness. Salinity of this snow-ice was slightly lower at 8 psu than the sea ice itself, which had a typical bulk salinity of 12 psu in the top 5 cm, decreasing gradually to a mean salinity of 5 psu below 50 cm depth. At the beginning of the measurement period (21:30 hrs on day 203) an ice core was removed for salinity (see Figure 11a) enabling brine volume and temperature calibration and a thermistor string to be emplaced and frozen into the core hole. Temperature, salinity and density measurements from the original core were used to derive a set of initial conditions in the ice sheet. Thereafter, thermistor string measurements were used to derive new values of the brine volume profile as the thermal profile adjusted to the local flux regime (Figure 11b). Cores extracted at the end of the drift experiment confirmed that the salinity of the ice sheet had undergone negligible change, and that there had been no detectable redistribution of brine within the ice sheet, or brine drainage. This implies that the brine volume profile can be fairly accurately specified from the phase relations for sea ice by using a measured temperature profile. The density of the ice was fairly constant with depth, with a mean value of 905.7 kg/m<sup>3</sup> and standard deviation of 14.45 kg/m<sup>3</sup>.

Snow conditions at the start of the experiment were optimal for the experiment, with minimal natural spatial variation in snow cover. Measurements along a line oriented in the direction of the scatterometer scan swath indicated a mean depth of 4.3 cm (excluding snow-ice) and a normal distribution of snow depths with a standard deviation of  $\pm 1.9$  cm. A strong negative thermal gradient of  $> 1^\circ/\text{cm}$  at the time of thermistor string emplacement had encouraged regenerative basal depth hoar formation in a layer of 1-2cm thickness and density of 300 kg/m<sup>3</sup>, with angular crystals of 1 mm mean diameter. Basal snow had salinities ranging from 8-20 psu likely due to brine wicking. Above this low density layer was a 2-3 cm layer of snow of 400 kg/m<sup>3</sup>. This snow comprised fine, densely packed windblown broken crystals with clusters of formerly sintered, angular stellar fragments. However, high initial densities had hindered depth hoar formation and this layer was less altered by temperature-gradient metamorphism. Salinities in this layer were also much reduced with a mean value of 2 psu. At the very surface of the snowcover was an 0.5 cm thick crust of high density snow with tiny broken crystals bonded

together by the effects of solar-noon heating and wind. This layer was too thin to be effectively sampled for snow density, but is estimated to have a density of around 700 kg/m<sup>3</sup> since it was hard enough to prevent footprints. Samples of the crust indicated negligible salinity on the first two days, but wind-blown salt spray from nearby leads is the hypothesised cause of typical observed surface salinities of 2-3 psu by the end of the drift period. Fresh light snowfall was observed on two occasions during the drift station, however, no net accumulation was observed.

### 6.3 Flux and Backscatter Observations

In Figure 12, data are compared for a period when the net radiation budget shows a large transition. 10 minute averages of wind stress and turbulent sensible heat flux together with the net energy budget during a C-band radar scatterometer time-series of measurements between days 203 and 206 (21 to 24 July, 1992) are shown. In the lowermost panel of Figure 12 the 45° incidence mean C-band signature is plotted starting at Julian Day 203.79. The solid line represents the mean VV-polarized backscatter ( $\sigma_{vv}^0$ ) with error bars indicating the maximum range of variability of independent data samples. A dotted line shows the corresponding mean HV polarized backscatter ( $\sigma_{hv}^0$ ). A 10 dB variation in  $\sigma_{vv}^0$  and 5 dB variation in  $\sigma_{hv}^0$  is observed in response to the changes in the heat fluxes presented.

Figure 12a indicates a large variation in wind stress (TAU) during this period, increasing rapidly to over 0.5 N/m<sup>2</sup> when the wind velocities (VEL) peaked at 20 m/s. The increase in wind velocity took place together with a large rise in air temperature (T) (Figure 12c) from around -23°C to 0°C, during the arrival of a warm front. As a consequence of the overcast skies, warm temperatures and the high wind, the sonic-anemometer-thermometer recorded a net downward (negative in sonic coordinate system) flux of sensible heat which peaked during the strong winds at 60 W/m<sup>2</sup>. Later, a sharp decrease in the amount of incoming turbulent sensible heat occurs on the morning of 24 July, during clear night skies.

A net energy budget ( $F_{NET}$ ) is shown in Figure 12c as a solid line, using a conventional system of negative net outgoing flux of heat and positive net incoming heat flux. The largest measured components of this budget are as indicated the net radiative flux (Q), the net sensible heat flux (H), and the conductive heat flux ( $F_{COND}$ ). At the beginning of the period, the surface lost nearly 50 W/m<sup>2</sup> in radiative and sensible heat with the loss balanced largely by heat conduction upward from the base of the ice. The conductive heat flux is maintained primarily by a large temperature gradient between the freezing temperature of water at the base (~-1.7°C), and a measured snow-ice interface temperature of -20.0°C. Only small amounts of latent heat is supplied by freezing at the base of the ice, as indicated by ice core measurements and the thermistor string. Immediately the sky became overcast on day 204 air temperatures began to rise and light snow started to fall. In Figure 12d initially the air-surface temperature difference climbs to 5°C. The snow cover

reacted accordingly, becoming briefly isothermal at  $-9^{\circ}\text{C}$  by day 204.85, as air temperatures attained a similar value. Thereafter, the snow surface temperature closely mimicked the air temperature and the snow temperature gradient became positive for the remainder of the time. Reversal of the snow and ice thermal gradient in the upper 40 cm of the ice also accounts for the reversal in  $F_{\text{COND}}$  at day 204.75.

During the period immediately following arrival of the warm front ( $\sim$  day 204.5) radar data in Figure 12d indicate several orders of magnitude variability in backscattering. The sharp reduction in VV and HV-pol backscatter is strongly correlated with the change in heat flux regime as the net radiative and sensible heat flux ( $Q+H$ ) swings from outgoing to incoming. The  $\sigma_{\text{VV}}^0$  reduction mirrors the corresponding fall in  $F_{\text{COND}}$  in Figure 12c, reaching a minimum below  $-35$  dB. On day 205, a reversal takes place in  $\sigma_{\text{VV}}^0$  with a rise in backscatter values up to a level higher than upon arrival on day 203. Subsequent high winds and a brief period of cloud-free night at Julian Day 206.25 encourage evaporative cooling and negative values of  $F_{\text{NET}}$ . A further local minimum in the values of VV and HV-pol backscatter occurs shortly afterwards, as  $F_{\text{NET}}$  turns positive at the end of the drift measurement period.

#### 6.4 Backscatter Response to Snow and Ice Conditions

The initial backscattering situation, characterised by air temperatures below  $-20^{\circ}\text{C}$  and relatively stable  $\sigma_{\text{VV}}^0$  backscatter of  $-30$  dB up to day 204.5, is modelled by Drinkwater *et al.* (1993) using a layered rough-surface and volume scattering model. Though the rough wind-packed crust plays an important role in terms of scattering the downward propagating beam (and potentially in generating a coherent component of backscatter for uniform thickness crusts), model results confirm the snow to be largely transparent at C-band with the primary scattering originating from the snow-ice interface. Permittivity and particularly the roughness of the ice surface are initially the important controls upon the magnitude of backscattering. At  $45^{\circ}$  a small non-negligible component of backscatter also originates from snow crystal scattering, due to the large crystals observed in the basal hoar frost layer.

Surface measurements in association with the C-band radar data help explain the change in the VV-polarized signal when air temperatures climb above  $-20^{\circ}\text{C}$ . After the warm front passes, conducted heat is expended by raising the temperatures in the upper 40 cm of the sea ice. Brine volumes in the upper 5cm of ice exponentially increased from 40-50 psu on day 203, to 80 psu by the end of day 204 (Figure 11b) and with a smooth thin blanket of fresh snow the air-snow temperature difference disappears. As ice-surface temperatures rise, the decay in  $\sigma_{\text{VV}}^0$  is largely driven by the increase in reflection coefficient caused by increasing brine volumes at the smooth ice surface. Acceleration in the decay is also correlated strongly with the appearance of destructive metamorphism after the snow acquires a positive temperature gradient at day 205.0.



This process was monitored using snow-grain macro-photography of samples collected during surface measurements. Photographs indicate that snow-grain transformations quickly proceed downwards into the snowpack, reducing the large angular positive metamorphism grains to extremely small rounded grains (0.1 - 0.3mm diameter) and thereby reducing the component of snow crystal volume scattering. Similarly, the thin blanket of cold, overnight fresh snow reduced the roughness and the reflection coefficient at the snow surface, lowering the rough surface scattering component. Each of these three effects results in a decline to a minimum in  $\sigma_{vv}^0$  and  $\sigma_{hv}^0$  at day 204.35, at around which time the overnight snowfall stopped.

Between day 205.4 and 205.5  $\sigma_{vv}^0$  undergoes a sharp reversal and rapid climb back to values around -30 dB. Correlated with this abrupt change is the rise of air temperature above 0°C, an increase in windspeed and relative humidity, and a further period of damp snowfall between 08:00 and 12:00 hrs. Warm air temperatures helped focus melt directly at the surface and downward heat conduction into the colder ice surface prevented significant melting lower in the snowpack. The initial sharp increase in surface permittivity, due to a thin damp surface layer, accounts for a sharp increase in both like and cross-pol scattering, and the variability in the  $\sigma_{vv}^0$  signifies rapidly changing surface conditions. During this period, no significant amount of surface wetness accumulated within the shallow snow layer until the latter part of day 205. Instead, wind speeds were high enough that sufficient heat is removed by surface sublimation to prevent visible melting and free-water appearance in the snow (as described by Andreas and Ackley 1982). Indeed, the net energy balance remains close to zero until day 205.5, and the continuing change in thermal profile promoted melt-freeze metamorphism and encouraged growth of larger rounded crystals and grain clusters. Together, it is proposed that these changes increase the level of rough surface scattering at the snow surface and restore volume scattering to a level commensurate with that first observed on day 203. More difficult to explain, however, is a second 3 dB drop in  $\sigma_{hv}^0$  which may be associated with the snow crystal rounding process, increases in snow layer absorption, or changes in surface roughness.

During the solar noon at day 205.65,  $F_{NET}$  turns positive for the first time and surface melting peaks. As the snow became damp, snow-surface scattering becomes a dominant source of backscattering. Correspondingly, snow absorption increases and ice surface scattering reduces in importance. At peak melt, the maximum surface wetness results in a peak in  $\sigma_{vv}^0$  at day 205.8, while second-order scattering effects within the snow, reflected by  $\sigma_{hv}^0$ , are reduced. A plateau in  $\sigma_{vv}^0$  lasts until air temperatures fall below zero once more around day 206.0, after which  $F_{NET}$  briefly turns negative.

This last significant change in backscatter takes place with a reduction in the turbulent heat flux during a cold, cloud-free period between 206.0 and 206.25. Persistent cold overnight

temperatures and reduced humidities encouraged rapid refreezing (day 206.25) of moisture in the snow layer. Diurnal cooling and the swing in the humidity during this period on day 206 (Figure 12b) result in a brief minima in  $\sigma_{vv}^0$ . However, data values measured with the scatterometer span the most critical period of refreezing, and it is speculated that the backscatter could (under the complete removal of moisture) have reached a minimum equivalent to that observed for dry snow with relatively large grains (i.e. the period between 205.0 and 205.2). The rapid return to values above -30 dB, at day 206.5, coincide with the brief period of incoming short-wave energy during scattered clouds at mid-day and signifies the reappearance of moisture at the surface of the snow with air temperatures above freezing.

The winter example presented clearly indicates that the snow and sea-ice surface properties respond sensitively to the balance of fluxes at the surface. Furthermore, C-band values of  $\sigma_{vv}^0$  react equally sensitively to these changes. In direct contrast to the winter Arctic situation, it is suggested that such temperature swings may indeed be a common situation for the Southern Ocean ice cover during winter, due to the high frequency of low pressure systems bearing warm moist air. This sequence in events may be recognized in time-series data to reflect transformations in the heat and vapour flux environment, or the onset of melting as has been demonstrated by Winebrenner *et al.* (1994) using Arctic ERS-1 SAR data.

## 7. Conclusions

More widespread field scatterometer measurements are required before Antarctic sea ice in the Weddell Sea and Southern Ocean in general is equally well characterised as Arctic sea ice, in terms of frequency- and polarisation-dependent microwave backscattering characteristics. Nonetheless, results presented here illustrate sea ice in the Weddell Sea to be somewhat unique in terms of its microwave backscattering signatures, and in that there is clearly much useful information to be derived by exploiting ERS-1 satellite active microwave data acquired in Antarctica. C-band scatterometer data samples from relatively thin first-year ice, and thicker deformed first-year ice or second-year ice are distinguishable in winter, thus providing a method for identifying relatively thin ice and therefore locations within the ice-pack where ocean-ice-atmosphere heat exchange is significant. Comparisons with calibrated ERS-1 SAR scenes show that these backscatter differences in the 20-26° incidence angle range can be used to discriminate thin and thick ice fairly effectively.

Drift-station C-band signatures show how the time dimension can be used to identify and signal changes in the surface flux environment, such as those accompanying the passage of frequent Antarctic low pressure systems. When coupled with air temperature measurements, these large variations in backscatter highlight key transitions in the surface fluxes associated with net ablation or ice growth. The dynamic range measured by the scatterometer during such cycling of

the heat fluxes indicates that significant information is contained at higher incidence angles such as 45°, where both surface scattering and volume scattering have a significant influence upon observed signatures. Future work will focus on quantifying the relationship between scattering albedo at C-band and the integrated optical albedo to see how closely they respond during the brief periods of ablation which accompany storm systems. It is proposed, with the aid of buoy data and weather analysis fields (for specifying boundary conditions), that satellite radar and surface energy balance data be used together with physical models to further investigate how microwave data reflect changes in the surface fluxes. The power of such time-series measurements using microwave backscatter has barely been exploited. Coupling microwave signature change analysis together with the tracking capability of SAR provides a powerful method for studying geophysical processes and surface changes throughout an entire Antarctic ice growth and decay season.

A complete regional and seasonal characterisation of the backscatter with both SAR and ERS-1 wind scatterometer data is of particular interest in the Weddell Sea (Drinkwater *et al.* 1994) since SAR provides high resolution information and the scatterometer provides complementary multiple incidence angle measurements with wider-scale coverage. Establishment and refinement of a methodology for application of such long-term spaceborne radar monitoring techniques is essential to the capability for estimation of the surface fluxes of the Weddell Sea and particularly evaluation of the impact of the entire Southern Ocean on global atmospheric and oceanographic conditions. When relationships between microwave signatures, geophysical properties and surface fluxes are understood in different heat flux regimes from surface experiments and/or autonomous surface instrument data, estimates may be extrapolated to larger scales over the Southern Ocean.

## **Acknowledgments**

Special thanks go to Robert Bruce for his efforts in preparing the data acquisition programs, and Wolfgang Dierking for support of the field measurements and in solving technical problems. Christian Haas, Alan Lohanick, Robert Massom and Markus Thomas are thanked for their untiring snow and ice data acquisition. Wolfgang Frieden of Hannover University and Christian Wamser of AWI kindly provided radiation and surface flux data, and Thomas Viehoff and Peter Lemke supported field measurement planning. M.R.D. carried out this work at the Jet Propulsion Laboratory, California Institute of Technology under contract to the National Aeronautics and Space Administration.

## **References**

ANDREAS, E. L., and ACKLEY, S. F., 1982, On the differences in Ablation Seasons of Arctic

and Antarctic Sea Ice, *Journal Atmospheric Science*, **39**, 440-447.

BEAVEN, S. G., and GOGINENI, S. P., 1994, Shipborne Radar Backscatter Measurements from Arctic Sea Ice During the Fall Freeze-Up, *Remote Sensing Reviews*, **9**, Harwood Academic Publishers, 3-25.

CARSEY, F. D., 1980, Microwave Observations of the Weddell Sea Polynya, *Monthly Weather Review*, **108**, 2032-2044.

CARSEY, F. D., BARRY, R. G., and WEEKS, W. F., 1992, Introduction, In *Microwave Remote Sensing of Sea Ice*, (editor) F.D. Carsey, AGU Geophysical Monograph , **28**, 1, 1-7.

DRINKWATER, M. R., and HAAS, C., 1994, Snow, Sea-ice and Radar Observations during ANT X/4: Summary Data Report, *AWI Berichte aus dem Fachbereich Physik*, **53** Alfred Wegener Institut für Polar- and Meeresforschung, July 1994, 58pp.

DRINKWATER, M. R., and KOTTMEIER, C., 1994, Satellite Microwave Radar- and Buoy-tracked Ice Motion in the Weddell Sea during WWGS'92. *Proceedings IGARSS '94*, **1**, Pasadena, CA, Aug. 8-12, 1994, 153-155.

DRINKWATER, M. R., EARLY, D. S., and LONG, D. G., 1994, ERS-1 Investigations of Southern Ocean Sea-ice Geophysics using Combined Scatterometer and SAR Images. *Proceedings IGARSS '94*, **1**, Pasadena, CA, Aug. 8-12, 1994, 165-167.

DRINKWATER, M. R., LONG, D. G., and EARLY, D. S., 1993a, Enhanced Resolution Scatterometer Imaging of Southern Ocean Sea Ice, *ESA Journal*, **17**, 307-322.

DRINKWATER, M. R., HOSSEINMOSTAFA, R., and DIERKING, W., 1993b, Winter Microwave Radar Scatterometer Sea Ice Observations in the Weddell Sea, Antarctica. *Proceedings IGARSS '93*, **2**, Tokyo, Japan, Aug. 18-21, 1993, 446-448.

GOGINENI, S., MOORE, R. K., WANG, Q., GOW, A., and ONSTOTT, R. G., 1990, Radar Backscatter measurements over saline ice, *International Journal Remote Sensing*, **11**, 603-615.

GORDON, A., 1991, Two stable modes of Southern Ocean Winter Stratification, Chu, P.C., and Gascard, J.C., (editors), *Deep Convection and Deep Water Formation in the Oceans*, Elsevier Science Publishers, 17-35.

GORDON, A., and HUBER, B. A., 1990, Southern Ocean Winter Mixed Layer, *Journal Geophysical Research* , **95**, 11655-11672.

GRENFELL, T. C., CAVALIERI, D. J., COMISO, J. C., DRINKWATER, M. R., ONSTOTT, R. G., RUBINSTEIN, I., STEFFEN, K., and WINEBRENNER, D. P., 1992, Microwave Signatures of New and Young Sea Ice, In *Microwave Remote Sensing of Sea Ice*, (editor) F.D. Carsey, American Geophysical Union, Geophysical Monograph **28**, Chap. 14, 291-301.

HAAS, C., VIEHOFF, T., and EICKEN, H., Sea Ice Conditions during the Winter Weddell Gyre Study 1992 ANT X/4 with R/V Polarstern: Shipboard Observations and AVHRR imagery, *AWI Berichte aus dem Fachbereich Physik*, **34**, Alfred Wegener Institut für Polar- und Meeresforschung, Dec. 1992.

HOSSEINMOSTAFA, R., LYTLE, V. I., JEZEK, K. C., GOGINENI, S. P., ACKLEY, S. F., and MOORE, R. K., In Press, Comparison of Radar Backscatter from Antarctic and Arctic Sea Ice, *Journal Electromagnetic Wave and Applications*.

KWOK, R. and CUNNINGHAM, G. F., 1994, Backscatter Characteristics of the Winter Ice Cover in the Beaufort Sea, *Journal Geophysical Research*, **99** (C4), 7787-7802.

LEMKE, P. (editor), 1994, The Expedition ANTARKTIS X/4 of R/V "Polarstern" in 1992, *Reports on Polar Research*, **140**, Alfred-Wegener-Institut für Polar- und Meeresforschung, D-27568, Germany, 90pp.

MARTIN, S., STEFFEN, K., COMISO, J., CAVALIERI, D., DRINKWATER, M. R., and HOLT, B., 1992, Microwave Remote Sensing of Polynyas, In *Microwave Remote Sensing of Sea Ice*, (editor) Carsey, F. D., American Geophysical Union, Geophysical Monograph **28**, Chapter 15, 303-311.

MOORE, R. K., 1985, Effect of Pointing Errors and Range on Performance of Dual-Pencil-Beam Scatterometers, *IEEE Transactions Geoscience and Remote Sensing*, GE-23, **6**, 901-905.

VIEHOFF, T., DIERKING, W., KOTTMEIER, C., and DRINKWATER, M. R., 1993, Sea ice characteristics in the Weddell Sea as observed by ERS-1 SAR, AVHRR, and ground-based measurements, Paper submitted to *Proceedings European Geophysical Society XVIII General Assembly*, Wiesbaden, Germany, 3 - 7 May.

WADHAMS, P., LANGE, M. A., and ACKLEY, S. F., 1987, The ice thickness distribution across the Atlantic sector of the Antarctic Ocean in mid-winter, *Journal Geophysical Research*, **92**, **14**, 535-552.

WINEBRENNER, D. P., NELSON, E. D., COLONY, R., and WEST, R. D., 1994, Observation of Melt Onset on Multiyear Arctic Sea Ice Using the ERS-1 SAR, *Journal Geophysical Research*, In Press.

## Tables

Table 1. System Specifications

---

Make:	King KRA 405 Radar		
Type:	Frequency Modulated Continuous Wave (FM-CW)		
Power Requirement:	28 VDC capable of 1.5 AMP output		
Transmitter Power:	150 mW		
Center Frequency:	4.3 GHz $\pm$ 15 MHz		
RF Bandwidth:	100 MHz		
Max/Min Hi/Lo Logic:	+10V --- +2V		
Polarization:	VV, HV		
Antennas:	Parabolic Transmit, Horn Receive (linear pol)		
Flat Plate KA 54 antenna (cross pol)			
Antenna Beamwidths:			
Transmitting (linear pol)	Parabolic:	E-plane;	8° elevation (circular)
	46cm diam.	H-plane;	8° azimuth (circular)
Receiving (linear pol)	Horn:	E-plane;	23° elevation
		H-plane;	22° azimuth
(cross pol)	KA 54:	E-plane;	50 $\pm$ 5°
		H-plane;	40 $\pm$ 4°
Calibration: Internal	Signal Injection (delay line)		
External	12" Luneberg-lens reflector		
Target Range:	15m - 60m		

---

## Figures

Figure 1. Weddell Sea study region showing shipborne scatterometer measurement locations and ice types.

Figure 2. Radar scatterometer mounted on port rail of *Polarstern* during WWGS '92.

Figure 3. 4.3 GHz FM-CW Radar Block Diagram.

Figure 4. (a) Antenna patterns of the v-pol transmitting and receiving antennas; and (b) illuminated area and beam-overlap on the surface (to scale).

Figure 5. (a) Internal 'feed-through' power variations over the period of WWGS '92 measurements; and (b) illustration of the IF Gain correction as a function of incidence angle.

Figure 6. (a) Pancake ice signature comparison between 13 and 14 June, 1992 near the ice margin; and (b) mean White ice signatures at VV- and HV-polarizations.

Figure 7. Comparison of medium first-year ice signatures at the same location (a) on 21 June, 1992 - before ridging (smooth), and (b) on 22 June - after ridging (rough).

Figure 8. Mean backscatter signature from combined measurements of smooth, medium-thick first-year ice.

Figure 9. Comparison of mean VV-pol. backscatter signatures of (a) rough first-year, and (b) second-year ice.

Figure 10. ERS-1 calibrated SAR backscatter distributions for rough first-year (FYR), smooth first-year (FYS), and mixed first- and second-year ice (FY/SY).

Figure 11. Ice core properties indicating (a) a comparison of initial (•) and final (˘) salinity profiles, and (b) the progression of brine volume changes associated with the temporal adjustment of temperature profile.

Figure 12. Comparison of shipborne C-band microwave radar scatterometer time-series with measured surface fluxes. (a) wind velocity (VEL) and turbulent flux of momentum (TAU); (b) turbulent flux of sensible heat (SENS HT) and humidity (HUMIDITY); (c) the net energy balance ( $F_{NET}$ ) with components of conductive ( $F_{COND}$ ) and radiative and turbulent ( $Q+H$ ) fluxes, and air temperature ( $T_{AIR}$ ); and (d) VV and HV-pol backscatter response, with snow-ice interface temperature (SNOW-ICE) and temperature difference between the air and surface ( $T_{DIFF}$ ).

**Running Headline Title:**

C-BAND BACKSCATTER FROM ANTARCTIC WINTER SEA ICE

C-BAND BACKSCATTER FROM ANTARCTIC WINTER SEA ICE

C-BAND BACKSCATTER FROM ANTARCTIC WINTER SEA ICE

C-BAND BACKSCATTER FROM ANTARCTIC WINTER SEA ICE

C-BAND BACKSCATTER FROM ANTARCTIC WINTER SEA ICE

C-BAND BACKSCATTER FROM ANTARCTIC WINTER SEA ICE

C-BAND BACKSCATTER FROM ANTARCTIC WINTER SEA ICE

C-BAND BACKSCATTER FROM ANTARCTIC WINTER SEA ICE

C-BAND BACKSCATTER FROM ANTARCTIC WINTER SEA ICE

C-BAND BACKSCATTER FROM ANTARCTIC WINTER SEA ICE

C-BAND BACKSCATTER FROM ANTARCTIC WINTER SEA ICE

C-BAND BACKSCATTER FROM ANTARCTIC WINTER SEA ICE



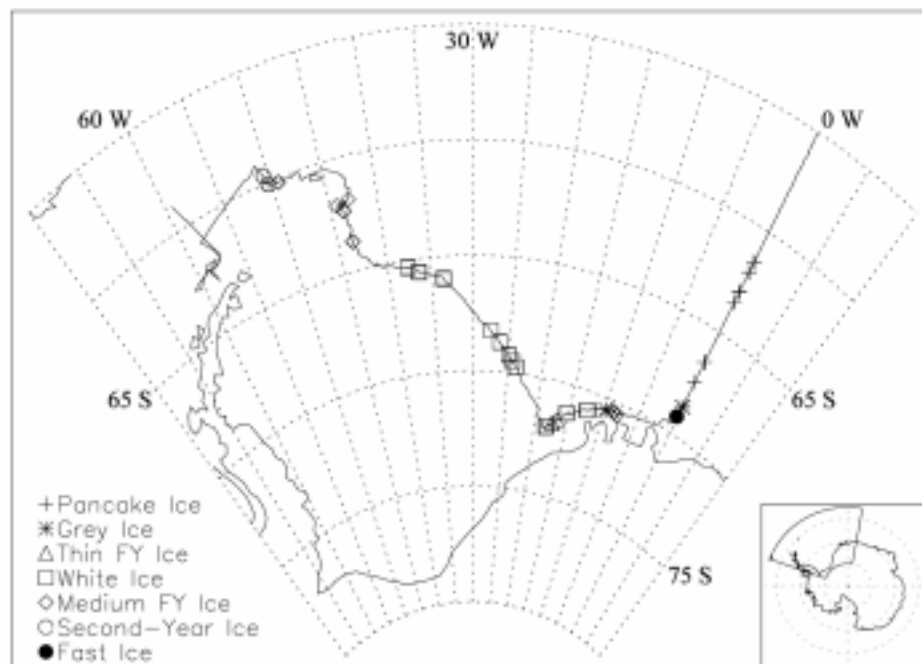


Figure 1. Weddell Sea study region showing shipborne scatterometer measurement locations and ice types.



Figure 2. Radar scatterometer mounted on port rail of *Polarstern* during WWGS '92.

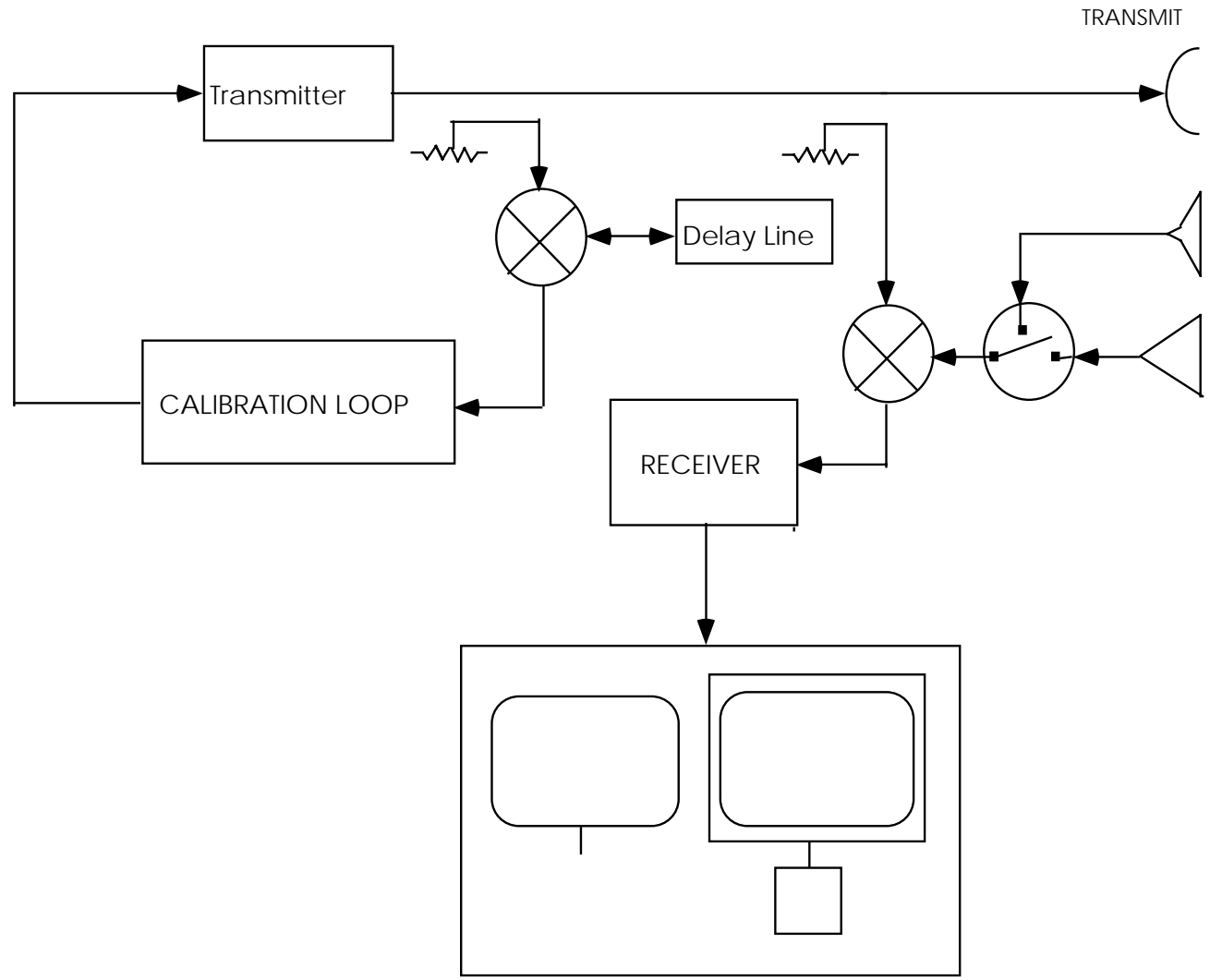
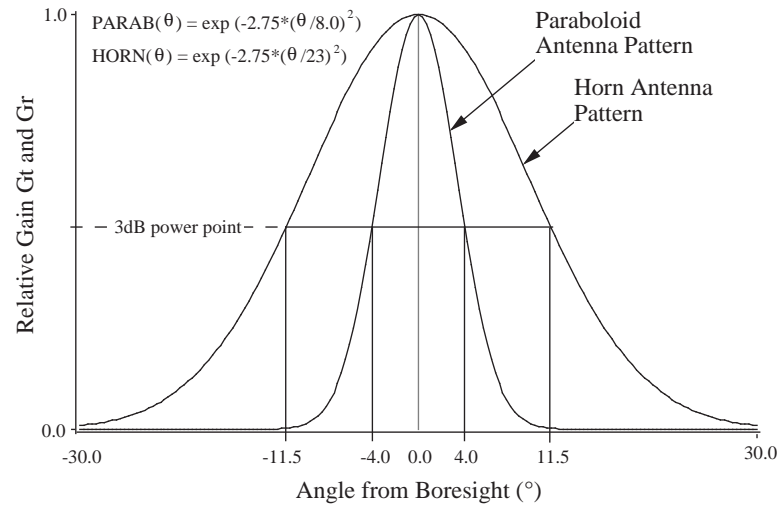


Figure 3. 4.3 GHz FM-CW Radar Block Diagram.

a



b

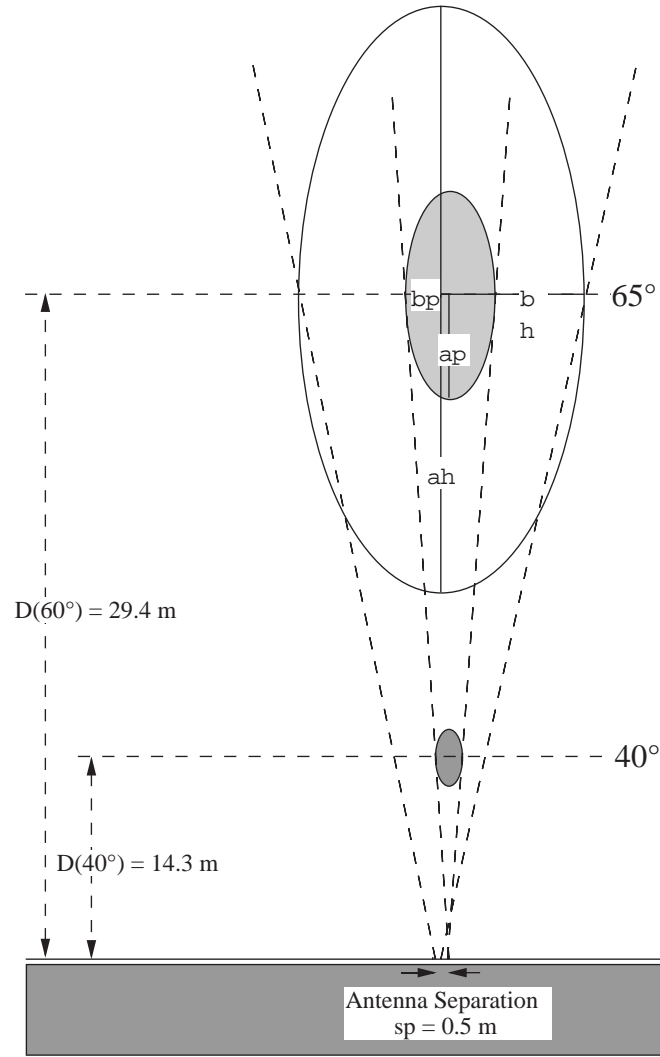
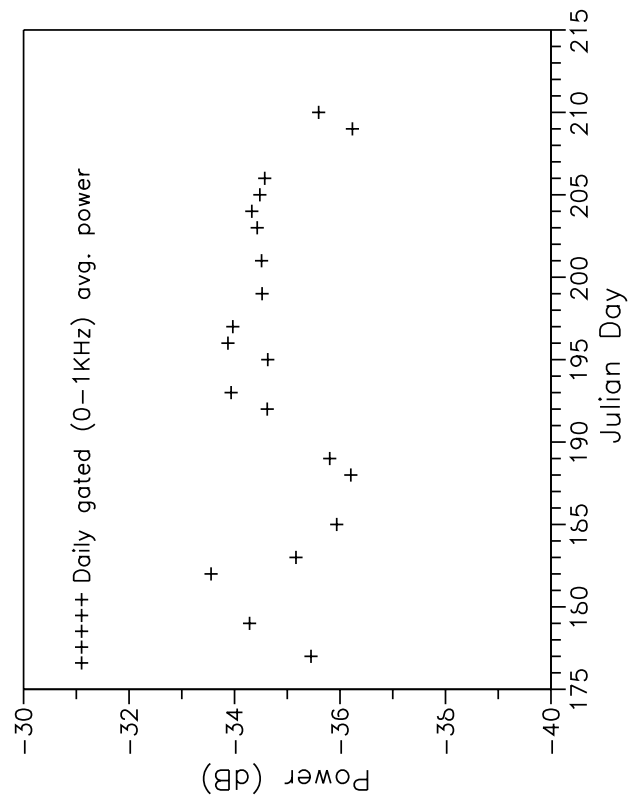


Figure 4. (a) Antenna patterns of the v-pol transmitting and receiving antennas; and (b) illuminated area and beam-overlap on the surface (to scale).

a.



b.

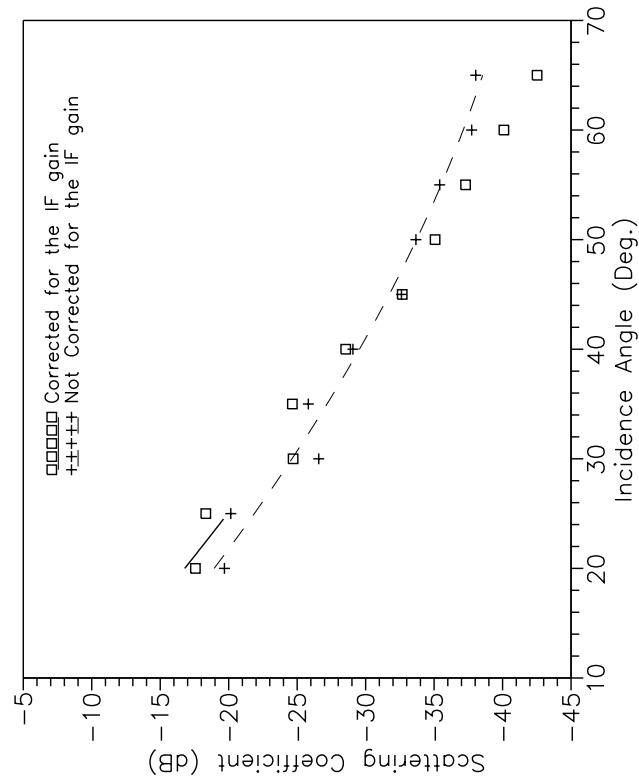
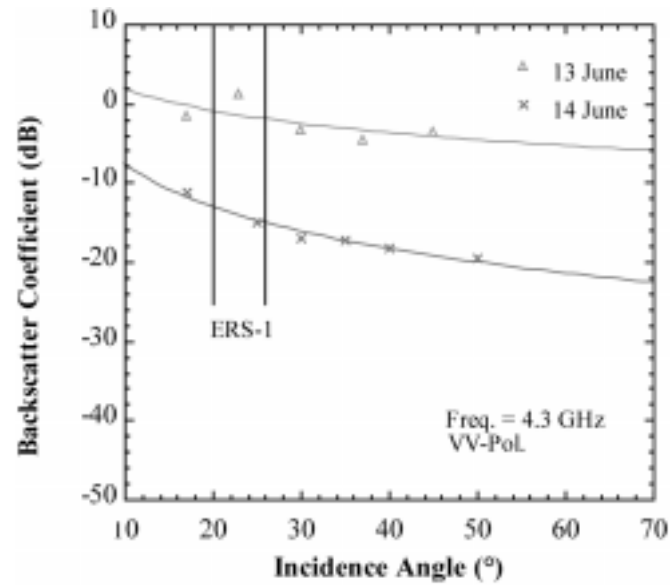


Figure 5. (a) Internal 'feed-through' power variations over the period of WWGS '92 measurements; and (b) illustration of the IF Gain correction as a function of incidence angle.

a.



b.

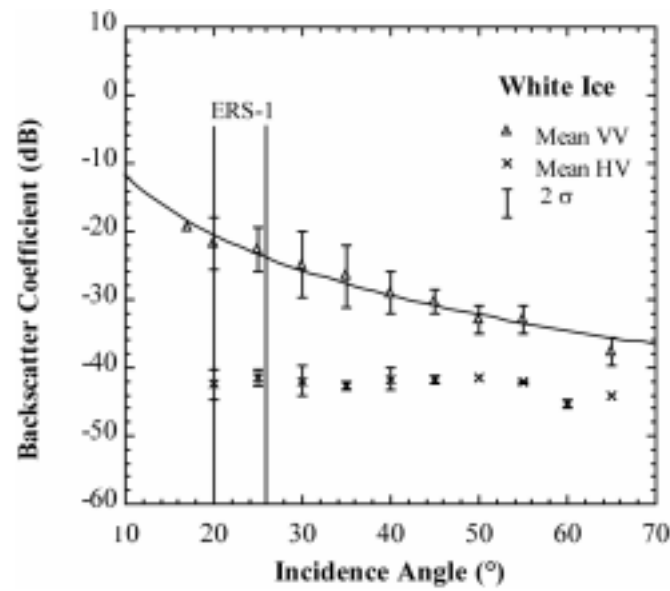


Figure 6. (a) Pancake ice signature comparison between 13 and 14 June, 1992 near the ice margin; and (b) mean White ice signatures at vv- and hv-polarizations.

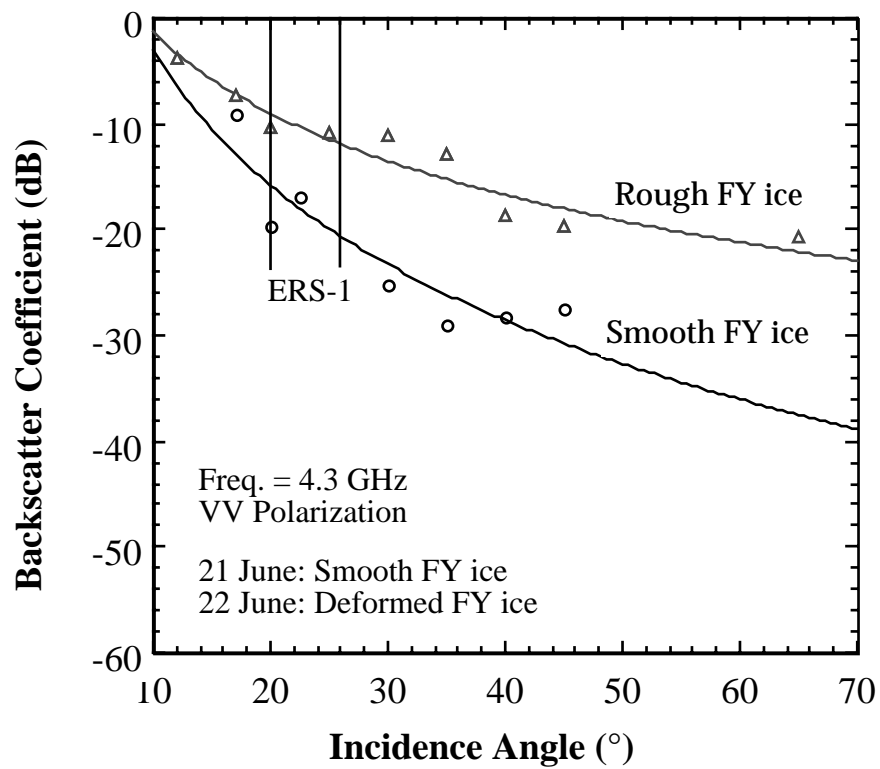


Figure 7. Comparison of medium first-year ice signatures at the same location (a) on 21 June, 1992 - before ridging (smooth), and (b) on 22 June - after ridging (rough).

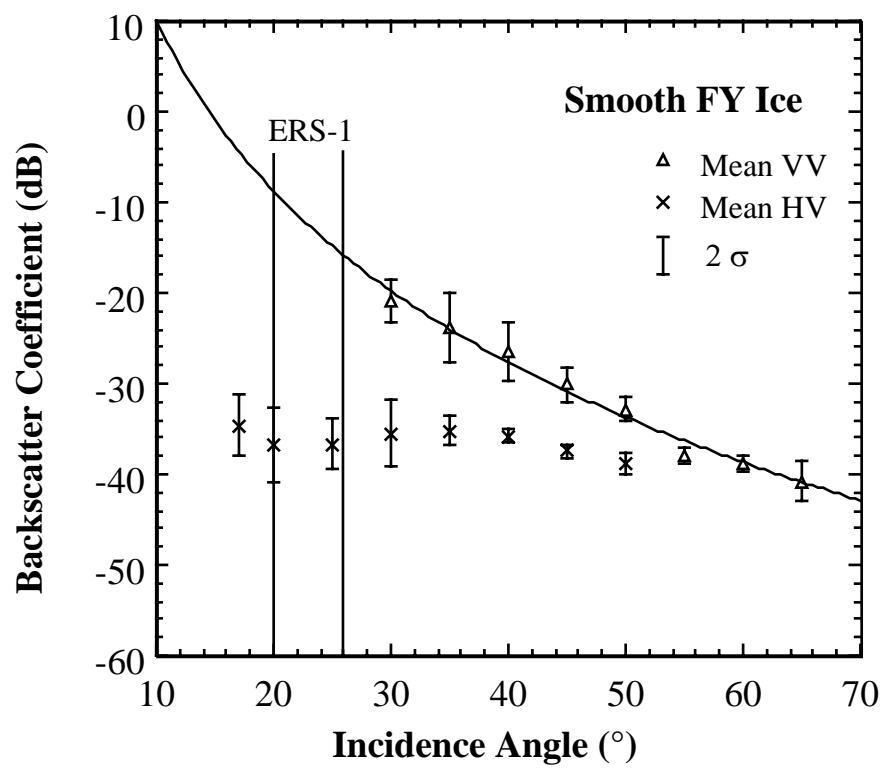
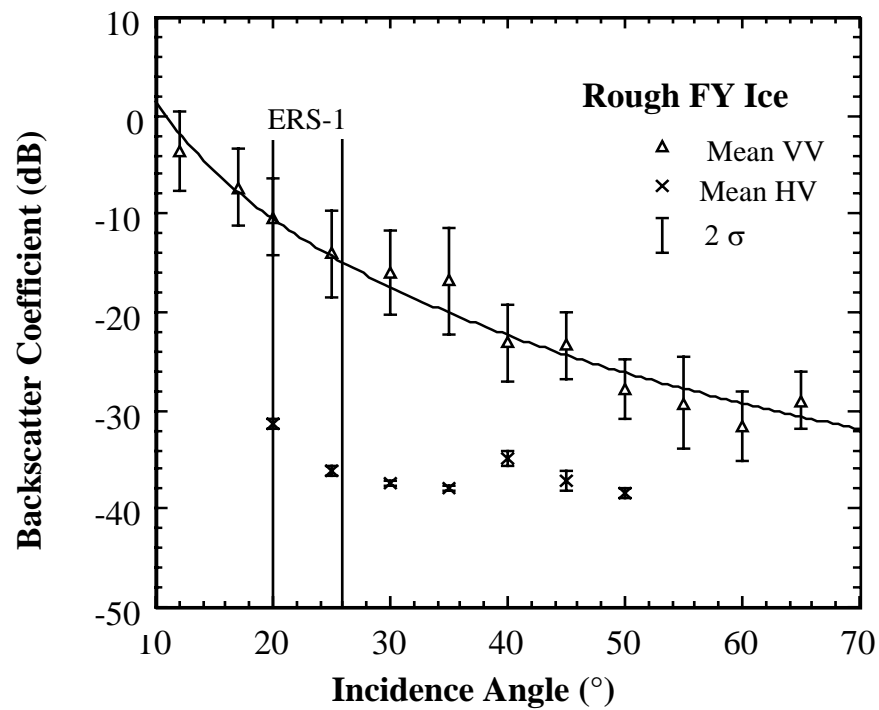


Figure 8. Mean backscatter signature from combined measurements of smooth, medium-thick first-year ice.



a



b.

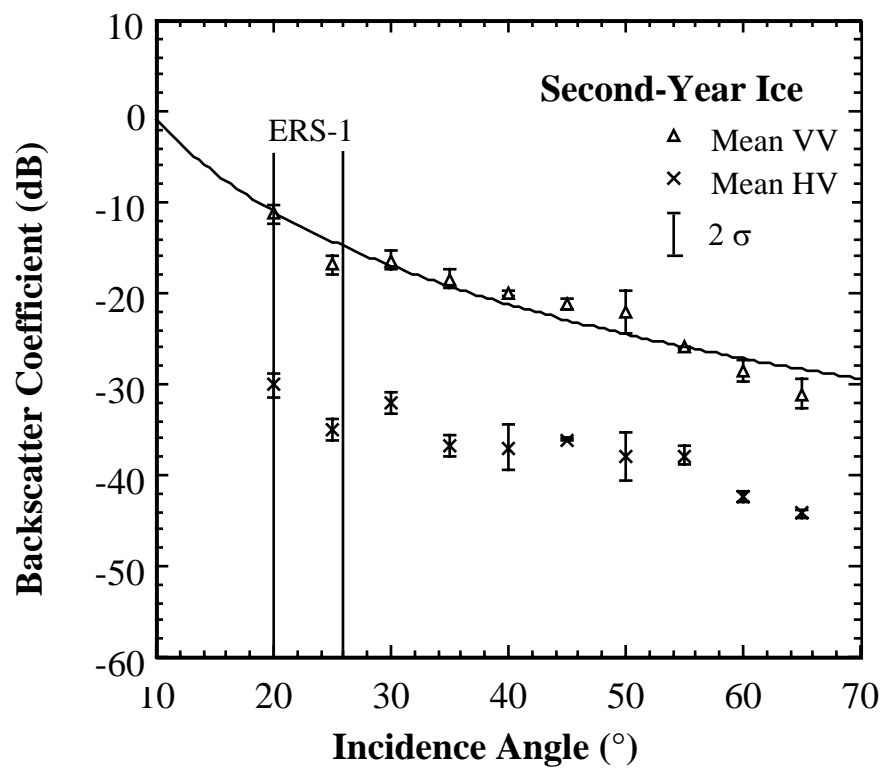


Figure 9. Comparison of mean vv-pol. backscatter signatures of (a) rough first-year, and (b) second-year ice.

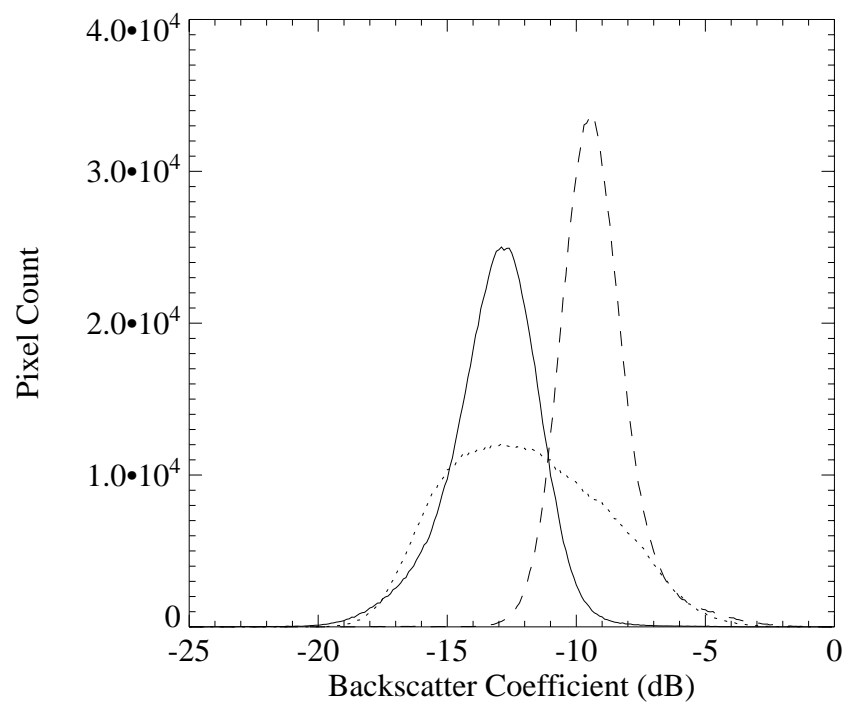


Figure 10. ERS-1 calibrated SAR backscatter distributions for; rough first-year (FYR); smooth first-year (FYS); and mixed first- and second-year ice.

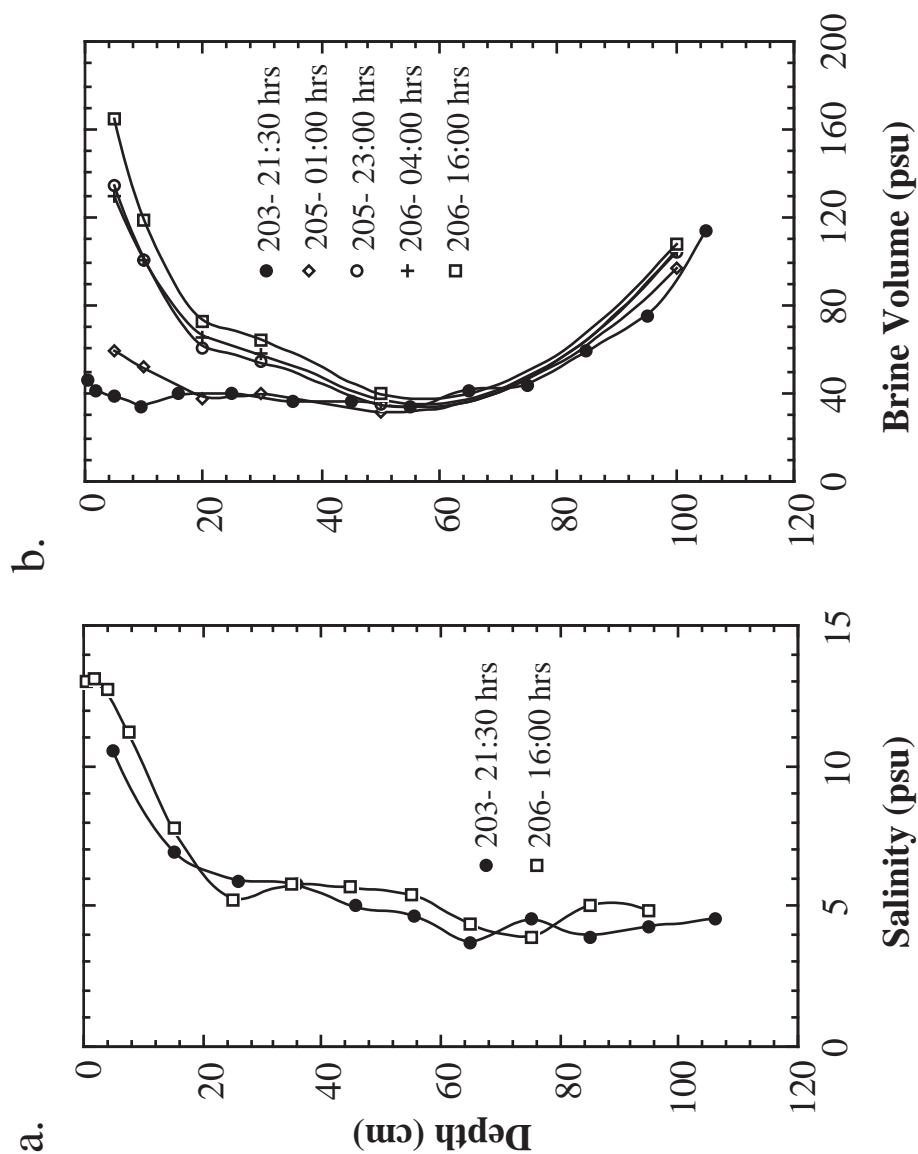


Figure 11. Ice core properties indicating (a) a comparison of initial (●) and final (◻) salinity profiles, and (b) the progression of brine volume changes associated with the temporal adjustment of temperature profile.

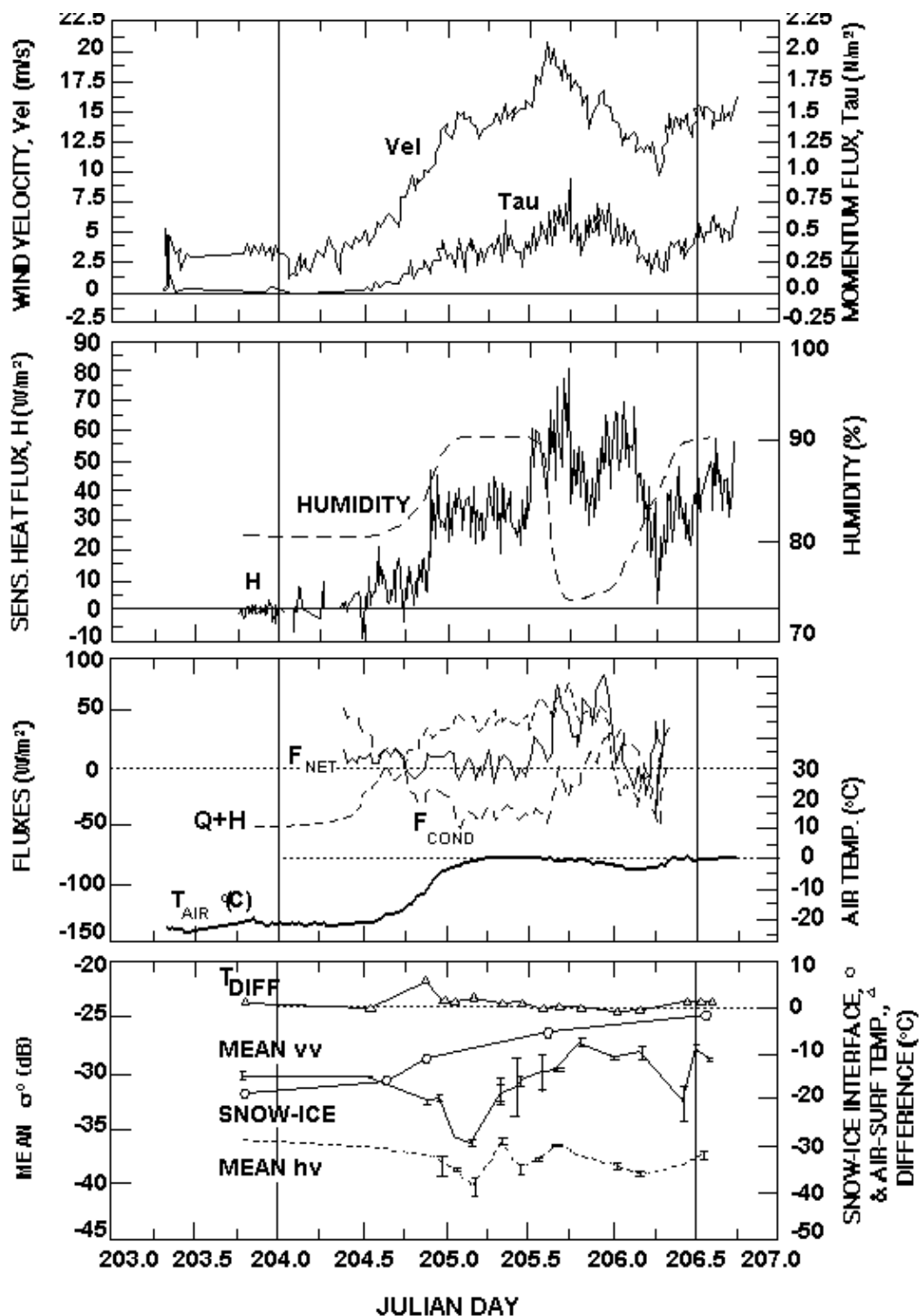


Figure 12. Comparison of shipborne C-band microwave radar scatterometer time-series with measured surface fluxes. (a) wind velocity (VEL) and turbulent flux of momentum (TAU); (b) turbulent flux of sensible heat (SENS HT) and humidity (HUMIDITY); (c) the net energy balance ( $F_{\text{NET}}$ ) with components of conductive ( $F_{\text{COND}}$ ) and radiative and turbulent ( $Q+H$ ) fluxes, and air temperature ( $T_{\text{AIR}}$ ); and (d) VV and HV-pol backscatter response, with snow-ice interface temperature (SNOW-ICE) and temperature difference between the air and surface ( $T_{\text{DIFF}}$ ).